In-Orbit External Calibration Method for Synthetic Aperture Radiometer

Jiakun Wang, Yinan Li, Wenxin Chen, Pengju Jin, Hailiang Lu, Xiaojiao Yang, Guangnan Song, Pengfei Li, Hao Li, and Rongchuan Lv

***Abstract*—The effective calibration of systematic errors is a precondition for high-quality images from a synthetic aperture radiometer system. The receiving channel errors can be relatively well calibrated, but antenna errors cannot be calibrated effectively in-orbit. This article proposes an in-orbit external antenna error calibration method for synthetic aperture radiometers using external calibration point sources on the ground. Simulation and experimental results demonstrate the accuracy and feasibility of the method. The layout of on-ground calibration point sources was then explored. Our results indicate that is sufficient to adjust the power of the calibration point sources when SNR is 30 dB, and that the calibration requirements can initially be met with three calibration point sources. If better calibration effect is required, eight calibration point sources are sufficient. Nonrepeated and uniform azimuth angle schemes appear to be the optimal layout for operating the proposed method, but adjustments can be made as necessary to suit the situation at hand. Finally, a feasible implementation scheme was established. The proposed method has certain reference value in terms of image quality improvement and practical engineering applications.**

***Index Terms*—Antenna error, external calibration, in-orbit, synthetic aperture radiometer.**

I. Introduction

AS AN interferometric device, the synthetic aperture radiometer is often used to measure the microwave radiation emitted by a given substance. Interferometric measurement can reveal a visibility function by sampling the spatial frequency domain of the radiation brightness temperature distribution, which can be used to reconstruct the brightness temperature images via Fourier transform [1]. This technique was originally developed for radio astronomy and has been applied more recently to Earth remote-sensing [2]–[4]. The synthetic aperture radiometer has two prominent advantages over the traditional microwave radiometer: 1) It does not require mechanical scanning and can image instantaneously, and 2) the system has much lower volume and weight.

The first of these devices, the electronically steered thinned array radiometer (ESTAR) developed at the Goddard Space Flight Center (GSFC), is an L band radiometer that employs aperture synthesis to obtain resolution in the across-track dimension and the "real" antenna aperture in the along-track dimension. ESTAR was eventually replaced by the 2-D synthetic aperture radiometer (2D-STAR), which employs aperture synthesis in both dimensions [5]. The Remote Sensing Group of Helsinki University of Technology (HUT) has been developing microwave radiometers for remote-sensing applications since the 1970s; they carried out a preliminary study on microwave radiometer techniques including a 1.4-GHz aperture synthesis radiometer and a 36.5-GHz polarimetric radiometer. The first airborne data acquisition with the complete HUT-2D system was conducted in May 2005, demonstrating the system's capability to produce interferometric data [5]. The geostationary synthetic thinned array radiometer (GeoSTAR) was developed to provide high spatial resolution soundings of the Earth's atmosphere from the geosynchronous earth orbit (GEO) in discrete microwave bands from 50 to 180 GHz [6]. The spatial resolution of its temperature measurement exceeds 50 km, and that of its water vapor and rainfall measurement is better than 25 km [7]. After more than 30 years of research and development, synthetic aperture radiometer has achieved soil moisture and ocean salinity (SMOS) [8]–[10] as a fledged in-orbit application. SMOS consists of a satellite in a sun-synchronous orbit at about 770-km height carrying a passive L-band sensor called the microwave imaging radiometer with aperture synthesis (MIRAS) [11], [12].

In the synthetic aperture radiometer system, the calibration of systematic errors is a crucial precondition for high-quality imaging. Traditional calibration methods mainly focus on the nonideal error of each part of the system and correct them separately [1]. For instance, correlated noise injection [13] can be used to correct the amplitude and phase discordance of receivers. Methods which correct the error itself provide "internal calibration." Internal calibration methods are now widely used to calibrate receiver error and have satisfactory effects, but cannot be used to calibrate antenna errors. External calibration became an important research topic for this reason.

Manuscript received November 30, 2020; revised February 3, 2021 and March 1, 2021; accepted March 12, 2021. Date of publication March 17, 2021; date of current version April 14, 2021. This work was supported in part by the National Natural Science Foundation of China under Grant 41706204 and Grant 61901244, in part by the Young Innovation Foundation of XueSen Qian, and in part by the Independent Investigate Project of the China Academy of Space Technology (Xi'an) under Grant Y17-KJCX-04. *(Corresponding author: Jiakun Wang.)*

Jiakun Wang, Yinan Li, Wenxin Chen, Hailiang Lu, Xiaojiao Yang, Guangnan Song, Pengfei Li, Hao Li, and Rongchuan Lv are with the Radar Department, China Academy of Space Technology (Xi'an), Xi'an 710100, China (e-mail: jiakunna@qq.com; liyinan_cast@126.com; chenwx801@sohu.com; hust_lhl@163.com; xiaoqiao_0709@126.com; songguangnan328@126.com; lipengfei123@qq.com; cast504_lihao@163.com; roselinda_lrc@163.com).

Pengju Jin is with the Communication Technology Department, China Academy of Space Technology (Xi'an), Xi'an 710100, China (e-mail: 541526293@qq.com).

Digital Object Identifier 10.1109/JSTARS.2021.3066488

This work is licensed under a Creative Commons Attribution 4.0 License. For more information, see https://creativecommons.org/licenses/by/4.0/

The G matrix method [14] of external calibration can be regarded as a discrete mathematical model using a calibration source to image individual observation azimuths in the field of view (FOV). Its calibration link encompasses the whole process of generating visibility function from the element antenna to the receiving channel, so the system does not require additional calibration hardware to achieve the necessary precision. However, there are notable drawbacks to the G matrix method. Measurements are complex and require massive workloads, particularly in cases of 2D systems. The response cannot be obtained simultaneously as the noise source must be measured from different directions. The properties of the system fluctuate during the measurement process, which can affect the calibration and render inaccurate results. Further, this method can only be carried out on the ground; it is not capable of in-orbit calibration. There are currently synthetic aperture radiometer systems which generate a G matrix by combining the antenna pattern data measured on the ground with the receiving channel data obtained by in-orbit calibration. However, the antenna pattern measured on the ground can change in orbit, thus giving inaccurate imaging results.

Flat target transformation (FTT) [15] is another classical external calibration method which takes the "cold sky" as a uniform and stable brightness temperature reference scene; the aircraft is "flipped" to observe the cold sky periodically to calibrate the system. FTT does not require any additional hardware and can be used to calibrate the whole system, however, it has certain drawbacks as well. When the satellite is in the state of earth observation and conducts cold sky observation in orbit, there is a certain temperature change in the radiometer system which alters the system parameters. Further, the cold sky is regarded as a completely flat target though its brightness temperature is not actually completely uniform, thus introducing error in the calibration data.

This article presents an in-orbit external calibration method for synthetic aperture radiometers. The method is validated on simulation and experimental data. The layout of on-ground calibration point sources was explored and a feasible implementation scheme was established. It is shown to retain the advantages of external calibration while resolving the disadvantage of the G matrix method that it can only be used on the ground, making it suitable for in-orbit aircraft application. It also avoids the drawback to the FTT method which requires the aircraft to flip toward the cold sky.

II. Fundamental Principles of Synthetic Aperture Radiometer

The basic constructional unit of the synthetic aperture radiometer is the binary interferometer, as shown in Fig. 1. Its function is to measure multiple correlations between two omnidirectional antenna elements, giving samples of a function called the "visibility function" [16]. The two antenna elements in different position constitute a pair of baselines.

The synthetic aperture radiometer system is, in actuality, a set of binary interferometers sharing antenna elements. These

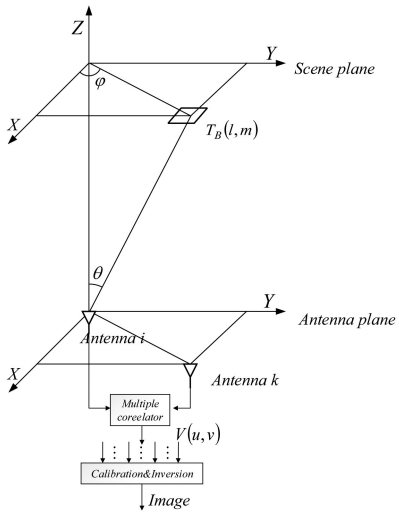

Fig. 1. Binary interferometer [17].

baselines in different lengths and directions cover different frequencies from low to high in the spatial frequency domain [17]. The relation between the visibility function and brightness temperature [15], when satisfying the far FOV condition, is

$$V_{ik}(u,v) = \iint_{\xi^2+\eta^2\le 1} T_{ik}(\xi,\eta)\tilde{r}_{ik}\left(-\frac{u\xi+v\eta}{f_0}\right)e^{-j2\pi(u\xi+v\eta)}d\xi d\eta \tag{1}$$

$$T_{ik}(\xi,\eta) = \frac{\sqrt{D_i D_k}}{4\pi}\frac{T_B(\xi,\eta)-T_r}{\sqrt{1-\xi^2-\eta^2}}F_{ni}(\xi,\eta)F^*{}_{nk}(\xi,\eta) \tag{2}$$

where

1) i and k are the labels of the two antennas in Fig. 1;
2) (u,v) are the baseline components of antenna i and antenna k normalized to the wavelength $\lambda{=}c/f_0$, with f_0 as the center frequency of the instrument ($u=\frac{x_k-x_i}{\lambda}$, $v=\frac{y_k-y_i}{\lambda}$);
3) $\xi=\sin\theta\cos\varphi$, $\eta=\sin\theta\sin\varphi$ is the directing cosine;
4) $T_B(\xi,\eta)$ is the brightness temperature;
5) $T_{ik}(\xi,\eta)$ is the modified brightness temperature;
6) $F_{ni}(\xi,\eta)$ and $F_{nk}(\xi,\eta)$ are normalized antenna voltage patterns of antenna i and antenna k;
7) $\tilde{r}_{ik}$ is the fringe-washing function related to the frequency response of the two receivers, which reflects the decorrelation effect of the system [18]; and
8) The terms D_i and D_k are the maximum directivity associated to the radiation from antenna i and antenna k, respectively.

Ideally, two different receiver channels perform exactly the same. The relative bandwidth of the system $B/f_0 \ll 1$. The fringe-washing function $\tilde{r}_{ik}(-\frac{u\xi+v\eta}{f_0}) \approx 1$. The relational expression between the visibility function and the brightness temperature distribution in the FOV is

$$V_{ik}(u,v) = \iint_{\xi^2+\eta^2\le 1} T_{ik}(\xi,\eta)e^{-j2\pi(u\xi+v\eta)}d\xi d\eta. \tag{3}$$

The visibility function and the brightness temperature are related by a Fourier transform

$$T(\xi,\eta) \underset{\text{IFFT}}{\overset{\text{FFT}}{\Longleftrightarrow}} V(u,v). \tag{4}$$

III. In-Orbit External Calibration Theory of Synthetic Aperture Radiometer

Synthetic aperture radiometer measurement technology depends on complex system hardware and signal processing in exchange for high spatial resolution. Compared with a traditional real aperture radiometer, the synthetic aperture radiometer system encounters a greater variety of errors. The system error may originate from antenna error and receiving channel error; the latter has been researched extensively and can be effectively corrected using existing techniques [19]. There is no fully sufficient technique for correcting antenna error, however, which also cannot be effectively calibrated in-orbit. As mentioned above, we focused on in-orbit antenna error calibration in this study. We focused on the antenna pattern error and antenna position error, which have the most serious impact among the various types of antenna error.

Amplitude error has little effect on the received signal, so, typically only the phase error effect is taken into account [20], [21]. According to the principle of the synthetic aperture radiometer, the signals received by the antennas first execute multiple correlation before further operation. Here, we focus on the relative error between antennas.

Once the relation between the visibility function $V(u,v)$ and the brightness temperature distribution in FOV $T_B(\xi,\eta)$ is obtained, we can assume that the phase error ΔC is only caused by the antenna pattern error $\Delta\theta$ and antenna position error Δu and Δv. Thus, the phase error originates in the $F_{ni}(\xi,\eta)F_{nk}(\xi,\eta)$ term and $e^{-j2\pi(u\xi+v\eta)}$. The ideal multiple correlation coefficient C_{ik} between antenna i and antenna k is given by

$$C_{ik} \Leftrightarrow f_i f_k^* e^{j2\pi[\xi(x_i-x_k)+\eta(y_i-y_k)]} \tag{5}$$

where, f_i and f_k are the patterns of antenna i and antenna k, respectively. Note that $\xi=\sin\theta\cos\varphi$, $\eta=\sin\theta\sin\varphi$. The multiple correlation coefficient of antennas i and k with antenna pattern and position error $\hat{C}_{ik}$ is

$$\begin{aligned}\hat{C}_{ik} \Leftrightarrow\ & f_i f_k^* e^{j(\Delta\phi_i-\Delta\phi_k)} e^{j2\pi[\xi(x_i-x_k)+\eta(y_i-y_k)]} \\ & \cdot e^{j2\pi[\xi(\Delta x_i-\Delta x_k)+\eta(\Delta y_i-\Delta y_k)]}\end{aligned} \tag{6}$$

where $\Delta\phi_i-\Delta\phi_k$ denotes the pattern phase error $\Delta\theta_{ik}$ of antennas i and k, while $\Delta x_i-\Delta x_k$ and $\Delta y_i-\Delta y_k$ denote the position errors Δu_{ik} and Δv_{ik}, respectively. Thus, the error of multiple correlation coefficient ΔC_{ik} attributable to the antenna pattern error and position error can be expressed as

$$\begin{aligned}\Delta C_{ik} \Leftrightarrow\ & e^{j(\Delta\phi_i-\Delta\phi_k)} e^{j2\pi[\xi(\Delta x_i-\Delta x_k)+\eta(\Delta y_i-\Delta y_k)]} \\ =\ & e^{j(\Delta\theta+2\pi\xi\Delta u+2\pi\eta\Delta v).}\end{aligned} \tag{7}$$

In order to determine the $\Delta\theta$, Δu, and Δv of the antenna pair, three known calibration point sources $P_1(\xi_1,\eta_1)$, $P_2(\xi_2,\eta_2)$, and $P_3(\xi_3,\eta_3)$ are randomly distributed on the ground. Equation (7) can be used to obtain the following relational expression:

$$\begin{cases}\Delta C_{12}^1 = \Delta\theta_{12}+2\pi\xi_1\Delta u_{12}+2\pi\eta_1\Delta v_{12} \\ \cdots \\ \Delta C_{ik}^m = \Delta\theta_{ik}+2\pi\xi_m\Delta u_{ik}+2\pi\eta_m\Delta v_{ik} \\ (i\neq k,\ m=1,2,3) \\ \cdots \\ \Delta C_{n(n-1)}^3 = \Delta\theta_{n(n-1)}+2\pi\xi_3\Delta u_{n(n-1)}+2\pi\eta_3\Delta v_{n(n-1)}\end{cases} \tag{8}$$

where n is the total number of antennas; ΔC^1, ΔC^2, and ΔC^3 are the multiple correlation errors of P_1, P_2, and P_3, respectively.

Now we can rewrite (8) in matrix form as (9). The dimensions of A, X, and C are $3(n-1)n*3(n-1)n$, $3(n-1)n*1$, and $3(n-1)n*1$, respectively.

The coefficient matrix A and the multiple correlation error matrix C can be obtained from the prior information directly to calculate the X matrix. Then, the pattern error $\Delta\theta$ and position error Δu, Δv between each antenna pair can be solved. Accordingly, the multiple correlation error of any unknown calibration point source $P(\xi,\eta)$ can be derived out through (10)

$$A\cdot X = C \tag{9}$$

$$A=\begin{bmatrix}1 & 0 & 2\pi\xi_1 & 0 & 2\pi\eta_1 & 0 \\ \ddots & & \ddots & & \ddots & \\ 0 & 1 & 0 & 2\pi\xi_1 & 0 & 2\pi\eta_1 \\ 1 & 0 & 2\pi\xi_2 & 0 & 2\pi\eta_2 & 0 \\ \ddots & & \ddots & & \ddots & \\ 0 & 1 & 0 & 2\pi\xi_2 & 0 & 2\pi\eta_2 \\ 1 & 0 & 2\pi\xi_3 & 0 & 2\pi\eta_3 & 0 \\ \ddots & & \ddots & & \ddots & \\ 0 & 1 & 0 & 2\pi\xi_3 & 0 & 2\pi\eta_3\end{bmatrix}$$

$$X=\begin{bmatrix}\Delta\theta_{12} \\ \vdots \\ \Delta\theta_{ik} \\ \vdots \\ \Delta u_{ik} \\ \vdots \\ \Delta v_{ik} \\ \vdots \\ \Delta v_{n(n-1)}\end{bmatrix},(i\neq k)\quad C=\begin{bmatrix}\Delta C_{12}^1 \\ \vdots \\ \Delta C_{ik}^1 \\ \vdots \\ \Delta C_{ik}^2 \\ \vdots \\ \Delta C_{ik}^3 \\ \vdots \\ \Delta C_{n(n-1)}^3\end{bmatrix},(i\neq k)$$

$$C_{ik} \Leftrightarrow \hat{C}_{ik} e^{-j\Delta\theta} e^{-j2\pi(\xi\Delta u+\eta\Delta v).} \tag{10}$$

The real multiple correlation matrix can then be obtained. After the redundancy of the real multiple correlation matrix is averaged, the calibrated visibility function can be obtained and inverted to determine the modified brightness temperature of the scene.

The feasibility and accuracy of the proposed method were verified by simulation using an array of 72 antennas distributed along a cross-shaped structure. Each of the 18 antennas were placed on one arm with an equal distance of 0.7 λ. The array layout is shown in Fig. 2.

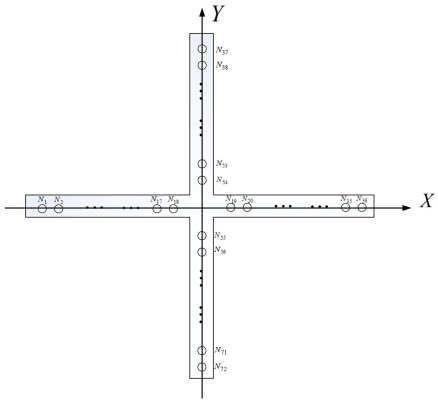

Fig. 2. Simulation model array.

In simulation, we added random error of 0–0.3 λ distributed to the position of each array element and random error of 0-$\pi/6$ rad distributed across the entire antenna pattern. We randomly selected three point sources in the FOV and selected a 30-dB signal-to-noise ratio (SNR) as the simulation condition. SNR $= 10\lg(\frac{T_N}{\text{NEDT}})$, where T_N denotes the apparent brightness temperature of the calibration source and NEDT denotes the sensitivity of the system.

We calibrated the added antenna pattern error and antenna position error by the proposed method. Fig. 3(a) shows the ideal image (without error) and Fig. 3(b) shows the image after adding random error to the position and pattern of each antenna array element. Fig. 3(c) shows the image calibrated by the proposed method. After adding error into the source, the brightness temperature is significantly offset compared to the image without error. After the calibration, the ideal image is basically restored, thereby verifying the effectiveness of the proposed method.

For further analysis, we subtracted Fig. 3(a) from Fig. 3(b) and (c) to observe the residuals between the ideal image and the image before and after calibration. Fig. 4 shows the results. The brightness temperature range of the residual error before calibration is about -45 to 45 k, and that after calibration decreases to nearly 0. The antenna error in Fig. 4(b) is corrected and the residual error is submerged in the sensitivity. This further demonstrates the strong calibration effect of the proposed method.

We further validated the proposed method by the root mean square error (RMSE), which reflects the deviation between measured and true values

$$\text{RMSE} = \sqrt{\frac{\sum_{i=1}^{n}\left(X_{\text{obs},i} - X_{\text{model},i}\right)^2}{N}} \tag{11}$$

With Fig. 3(a) as a standard, we calculated the RMSE of Fig. 3(b) and (c) for comparison. The results are listed in Table I.

As illustrated in Table I, the RMSE of the uncorrected image is rather large at 11.9482 K. After calibration, the value is markedly reduced to 0.8797 K; the error of the image is reduced by an order of magnitude. This implies that the serious distortion in the original scene is effectively, theoretically, managed by the proposed in-orbit external calibration method. We conducted a physical experiment to further test the proposed method, as discussed in detail below.

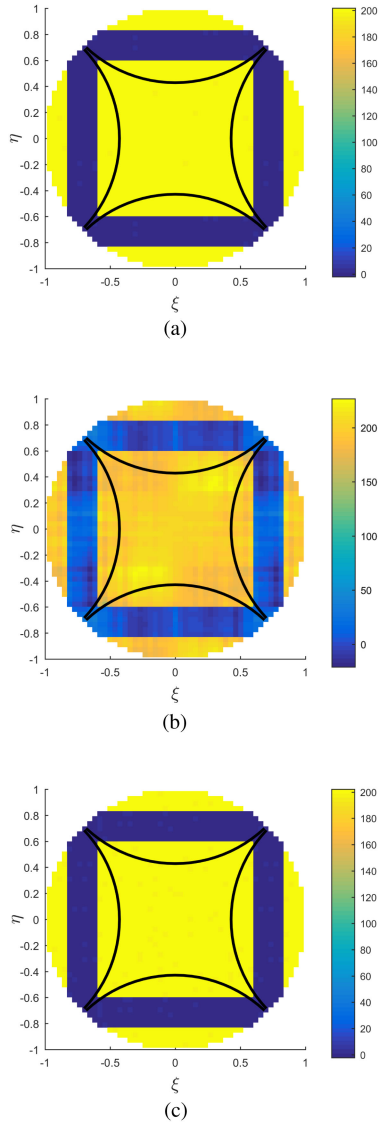

Fig. 3. Comparison of simulation results (30-dB SNR).

TABLE I
IMAGE RMSE BEFORE AND AFTER CALIBRATION

	Before Calibration(K)	After Calibration(K)
RMSE	11.9482	0.8797

IV. EXPERIMENTAL IN-ORBIT EXTERNAL CALIBRATION METHOD VERIFICATION

An outfield experiment was carried out on an X-band 2D synthetic aperture radiometer system to validate the proposed method beyond the simulation results discussed above.

The simulation model was established based on an ongoing project in our laboratory. We initially chose the same 72-element

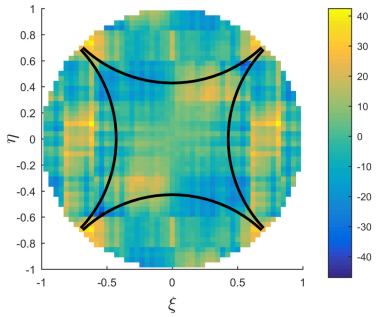

(a)

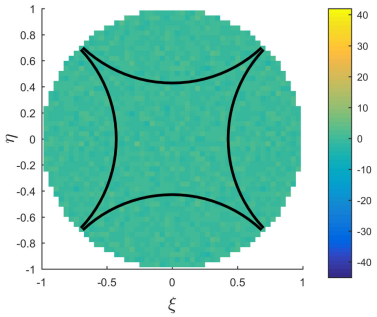

(b)

Fig. 4. Residuals before and after external calibration (30-dB SNR).

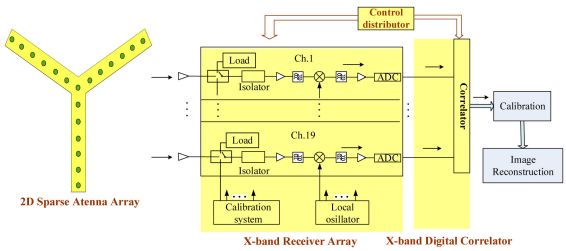

Fig. 5. X-band 2D synthetic aperture radiometer system composition block diagram.

cross-shaped array used in the simulation to structure the experiment. However, when the manuscript was submitted, the instrument had not been completely finished. We instead used an existing 19 element Y-shaped array [22] to verify this method. The proposed method is applicable to synthetic aperture radiometer antenna arrays of any shape, so the difference between the cross-shaped array and the Y-shaped array, as well as the difference in the number of antenna elements, do not affect the method itself. A block diagram of the experimental system is given in Fig. 5.

The experimental equipment is shown in Fig. 6. The two outmost antenna elements of each antenna arm were not used in the experiment. Table II lists the main technical indicators of the system.

The X-band noise source was chosen as the calibration source according to the X-band synthetic aperture radiometer. The calibration source was generated by connecting the antenna to the adjustable noise source component to transmit the calibration signal. The adjustable noise source component comprises a noise

Fig. 6. Experimental equipment composition of X-band 2D synthetic aperture radiometer system.

TABLE II
MAIN TECHNICAL INDICATORS OF EXPERIMENTAL SYSTEM

System Indicator	Parameter
Frequency	10.7 GHz
Bandwidth	100 MHz
Integration Time	1 s
Antenna Form	Y-shaped
Number of Antenna Elements	19
Antenna Unit Spacing	0.85 λ
FOV	50°
Resolution	4.2°
NEDT	0.11 K

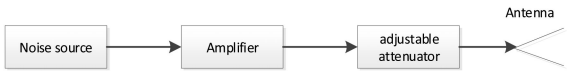

Fig. 7. Adjustable noise source component schematic diagram.

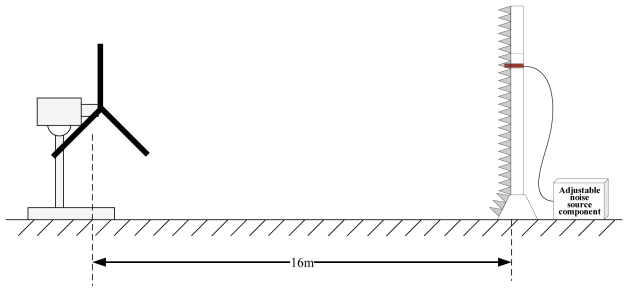

Fig. 8. Experimental equipment layout.

source, an amplifier, and an adjustable attenuator through which the output power of the calibration source signal can be adjusted (Fig. 7).

In the experiment, the calibration source was placed within the FOV and surrounded by an upright board affixed with absorbent material to eliminate any interference due to signal reflection (Figs. 8 and 9). The distance between the calibration source and the antenna array must satisfy the far-field condition, that is, $S \geq 2D^2/\lambda$, where D represents the antenna size. We set the distance to 16 m. We used a theodolite to determine the relative position between the calibration source and the instrument.

Fig. 9. Physical image of noise source.

The apparent brightness temperature of the calibration source T_N can be calculated as follows [23]:

$$T_N = \frac{1}{4\pi}(T_S - T_{ch})D(\theta,\varphi)\Omega_S \tag{12}$$

where T_S represents the brightness temperature at the calibration antenna port of the calibration source and T_{ch} is the temperature of the absorbing material. $D(\theta,\varphi)$ is the antenna directivity, $\Omega_S = A_r/R^2$ is the antenna space angle, A_r is the aperture size of transmitting antenna, and R is the distance from the calibration source to the antenna array.

In the experiment, the X-band 2D Y-shaped synthetic aperture antenna array first received the microwave radiation signal in the FOV to the 19-channel receiver array. The signal was then transmitted to a digital correlator for data processing and the visibility function of all baselines was generated through correlation operations. Next, the system performed internal and external calibration of the visibility function while internal calibration corrected channel crosstalk and amplitude inconsistencies. External calibration corrected antenna pattern errors and antenna position errors. Finally, the brightness temperature image was reconstructed by an image inversion operation.

Internal calibration must be processed before the external calibration begins, including calibration of the crosstalk between channels via noncoherent noise injection method and inconsistent calibration of the channel amplitude and phase via coherent noise injection method. In the experiment, we injected noncoherent noise by a matching load while high-temperature and low-temperature sources acted as calibration point sources for the coherent noise injection. After the internal calibration, we collected calibration point sources from different directions to verify the in-orbit synthetic aperture radiometer external calibration effectiveness. As discussed in Section III, at least three calibration point sources should be selected for this scheme. The azimuth angles of the three sources all differ.

We carried out the test on the roof of the A3 building of the China Academy of Space Technology (Xi'an). We used close-shot characters as the observation targets. The imaging results are shown as Fig. 10. Please note that absolute calibration was not performed, so the color values shown here are the count output values rather than the real brightness temperature.

The imaging results show that the character profile is not evident and the background is inhomogeneous after only internal calibration is performed. After the external calibration method is operated, the character profile can be clearly distinguished and the background is considerably more uniform.

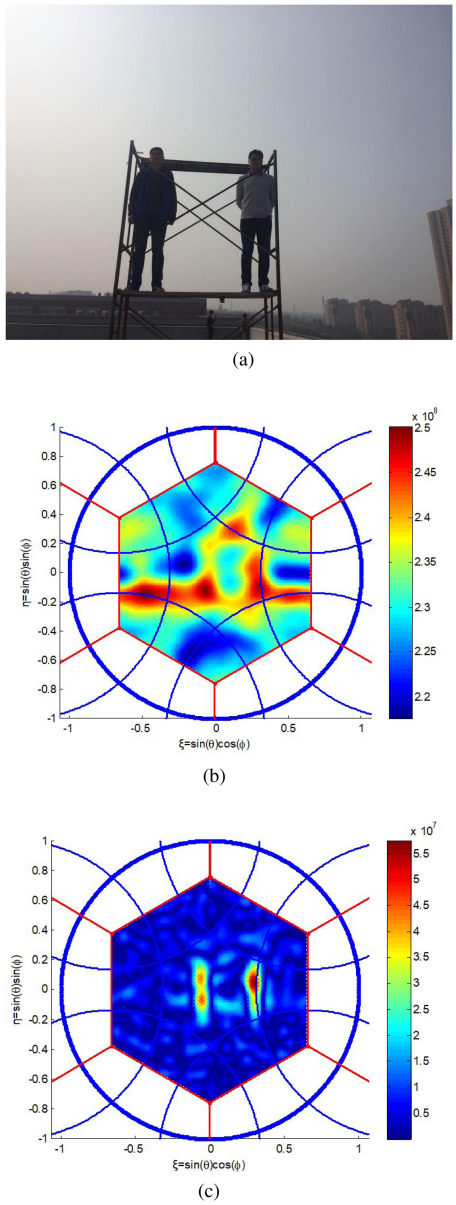

Fig. 10. Imaging results. (a) Optical image. (b) Image before external calibration. (c) Image after external calibration.

V. Implementation of In-Orbit External Calibration Method

We investigated the implementation of the proposed method using four performance indicators.

A. Calibration Source SNR

The SNR of the calibration point source is closely related to its power. In comparison with the environmental noise, the SNR of calibration point source received by the system is higher when the power is higher. In practice, external calibration is conducted

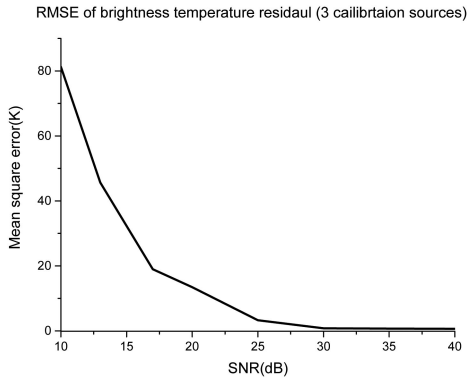

Fig. 11. Residual error of image with different SNRs (three calibration point sources).

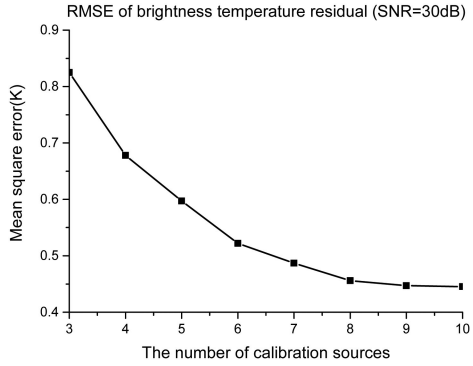

Fig. 12. Residual error of image in different calibration point sources (SNR = 30 dB).

in active transmission mode from the ground calibration point sources while the in-orbit synthetic aperture radiometer system passively receives the signal. For the ground calibration point sources to be observed, it is necessary to distinguish them from the background. The power should not be so large, however, that it causes other unwanted effects. We sought the appropriate SNR of the calibration point sources to strike this balance. We set three calibration sources as the simulation condition and used different SNRs (10 to 40 dB) to solve the system error. The mean square error values of the image brightness temperature residual after calibration were obtained accordingly.

Noise has less effect on inversion accuracy when SNR is high, thus improving the calibration result and imaging quality. As shown in Fig. 11, the residual of the image gradually decreases as SNR increases. When the SNR reaches 30 dB, it tends to be flat indicating near complete saturation. At this point, there is no significant reduction in image residuals as the SNR continues to increase. In practice, it would be sufficient to adjust the power of the calibration point sources when SNR reaches 30 dB.

B. Number of Calibration Point Sources

The minimum number of calibration point sources corresponds to the number of unknown parameters. That is, if there are N unknown parameters, at least N calibration sources to obtain a solution. The error terms to be solved include one antenna pattern error and two antenna position errors, so at least three calibration point sources are required. If the position error of the Z coordinate is introduced, the number of error terms increases to four and at least four calibration point sources are required (and so on).

Residual errors in the system imaging process result from antenna position errors, antenna pattern errors, and noise. The former two factors are deterministic errors and the latter one is a random variable. According to (11), increasing the number of calibration point sources makes the number of calibration sources greater than the number of unknowns, thereby transforming the equation into an overdetermination problem. We adopted the least squares criterion to solve the overdetermined equations in this study. More equations can enable the deterministic errors to be solved while weakening the influence of the noise term. The parameters to be solved are summed and superimposed, but the noise power is not included as the noise differs at each observation point and at different points in time. Therefore, more observation equations can reduce the influence of noise on the accuracy of the parameters to be solved while optimizing the system's imaging effect. However, the improvement is not inexhaustible. We determined the most suitable number of calibration point sources by simulating the brightness temperature residual as shown in Fig. 12.

The increase in the number of calibration point sources reduced the residual brightness temperature of the image in our case; the calibration effect on the image also grew less intense, especially beyond eight points. This implies that adding more calibration sources after the first eight does not significantly improve the calibration effect.

In practical applications, the calibration requirements can be initially met by using three calibration point sources. If better calibration effect is required, eight calibration point sources are sufficient. Continuing to increase the number of calibration point sources beyond eight remits no significant improvement in the calibration effects.

C. Layout Azimuth Repeatability

When the SNR and the number of calibration point sources are both determined, the calibration effects differ with different azimuths. The layout azimuth repeatability of the calibration data was investigated for this reason.

Two schemes emerge if more than three calibration point sources are used: 1) The azimuth angles of all calibration point sources are different and the layout azimuth of each set of calibration point sources is not repeated or 2) at least three azimuth angles of the calibration point sources are different and the others can repeat. "Repeated calibration point sources" mean that redundant equation conditions are identical, which can affect the accuracy of equation solutions.

We simulated and analyzed the calibration effects of both schemes. The brightness temperature residuals and mean square error values of the two schemes were obtained with 3–10 calibration point sources. As shown in Fig. 13, the two schemes both reduce the brightness temperature residual of the image as the number of calibration point sources increases. The mean

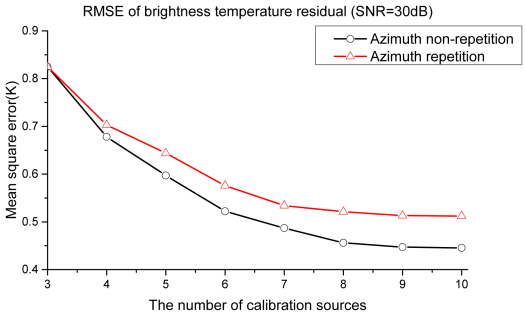

Fig. 13. Residual error of image with different azimuth angle repeatability (SNR = 30 dB).

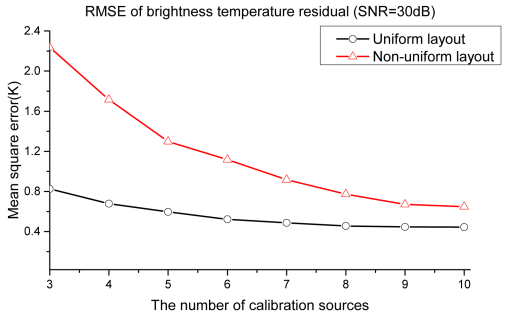

Fig. 15. Residual error of image with different azimuth angle uniformity values (SNR = 30 dB).

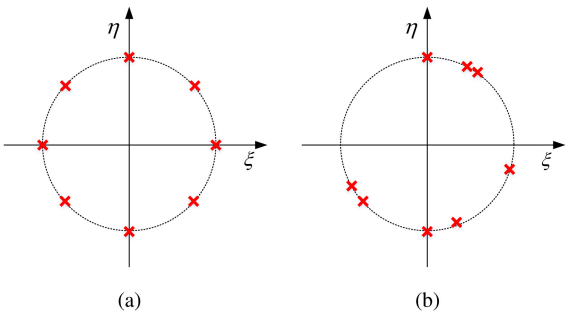

Fig. 14. Layout azimuth uniformity (eight calibration point sources). (a) Uniform layout. (b) Non-uniform layout.

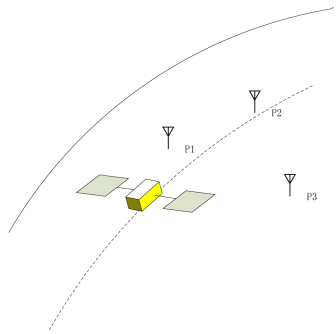

Fig. 16. Schematic diagram of calibration implementation.

square error value of the bright temperature residual after the azimuth nonrepetition scheme is smaller than that of the azimuth repetition scheme, that is, the azimuth nonrepetition scheme has better calibration effects though the azimuth angle repeated scheme seems more straightforward. However, to guarantee that the azimuth angle of each set of observations is repeated, the calibration point sources need to be alternately distributed on the parallel lines of the two aircraft's running trajectories. This significantly restricts the layout of the calibration point sources.

Overall, the azimuth angle nonrepeated scheme is recommended as it has better calibration effects and is relatively simple to implement.

D. Layout Azimuth Uniformity

There are two layout schemes available in the case of azimuth angle nonrepetition: 1) A uniform layout where N calibration sources are uniformly distributed in the observed azimuth and 2) a nonuniform layout where the values of the observed azimuth of N calibration sources are randomly distributed. Consider a scenario with eight calibration point sources as an example. The uniform layout of azimuth angles of all observed data is shown in Fig. 14(a) and the nonuniform layout is shown in Fig. 14(b).

Excessively concentrated calibration point sources make the equations too similar and coherent, thus affecting the accuracy of their solutions. We simulated the two layout schemes to observe the differences in their calibration effects. The mean square error values of the brightness temperature residuals were obtained with 3–10 calibration point sources.

As shown in Fig. 15, the two schemes both reduce the brightness temperature residual error as the number of calibration point sources increases, but the overall calibration effect of the uniform layout scheme is better. After 100 simulation iterations, a few relatively large values drive upward the average value as the observed azimuths of the points are very close. So, the difference seems significant at the beginning, but is slighter when a greater number of calibration sources is used. Uniform layout schemes should be given priority in practical applications to obtain more accurate calibration results. However, the uniform layout scheme has stricter requirements regarding the layout of calibration point sources. If the layout environment cannot be satisfied or the scheme is too complicated, corresponding adjustments can be made according to the situation at hand.

We designed a scheme for in-orbit external calibration of the synthetic aperture radiometer according to the observations discussed above. To obtain three unknown quantities $\Delta\theta$, Δu, and Δv between each pair of antennas, three calibration point sources $p_1(\xi_1, \eta_1)$, $p_2(\xi_2, \eta_2)$, and $p_3(\xi_3, \eta_3)$ are required. The calibration sources are noise sources, the bandwidths of which should slightly exceed that of the spaceborne synthetic aperture radiometer. According to (12), the power settings of the calibration sources must be selected so that the ratio of the apparent bright temperature to the system sensitivity is greater than 30 dB. The schematic diagram is shown in Fig. 16.

We first set a number of point sources that can be accurately located by GPS on the ground so that the aircraft could obtain their brightness temperature information from above. We calculated the multiple correlation coefficient error ΔC of the system itself

TABLE III
MATRIX RANK UNDER DIFFERENT PARAMETERS

No.	Condition of θ and φ	Rank(A)
(1)	$\theta_1 = \theta_2 = \theta_3, \varphi_1 = \varphi_2 = \varphi_3$	$(n-1)n$
(2)	$\theta_1 = \theta_2 \neq \theta_3, \varphi_1 = \varphi_2 = \varphi_3$	$2(n-1)n$
(3)	$\theta_1 \neq \theta_2 \neq \theta_3, \varphi_1 = \varphi_2 = \varphi_3$	$2(n-1)n$
(4)	$\theta_1 = \theta_2 = \theta_3, \varphi_1 = \varphi_2 \neq \varphi_3$	$2(n-1)n$
(5)	$\theta_1 = \theta_2 \neq \theta_3, \varphi_1 = \varphi_2 \neq \varphi_3$	$2(n-1)n$
(6)	$\theta_1 \neq \theta_2 = \theta_3, \varphi_1 = \varphi_2 \neq \varphi_3$	$3(n-1)n$
(7)	$\theta_1 \neq \theta_2 \neq \theta_3, \varphi_1 = \varphi_2 \neq \varphi_3$	$3(n-1)n$
(8)	$\theta_1 = \theta_2 = \theta_3, \varphi_1 \neq \varphi_2 \neq \varphi_3$	$3(n-1)n$
(9)	$\theta_1 = \theta_2 \neq \theta_3, \varphi_1 \neq \varphi_2 \neq \varphi_3$	$3(n-1)n$
(10)	$\theta_1 \neq \theta_2 \neq \theta_3, \varphi_1 \neq \varphi_2 \neq \varphi_3$	$3(n-1)n$

by comparison against the received information and the given information. According to the previous theoretical derivation, three points functionalize as a group. The error of the antenna pattern and the position error was calculated to correct the target brightness temperature information.

As per the theoretical basis given above, the A matrix of (9) needs to have full rank to obtain a unique error solution. Table III shows the results when A matrix is in the full-rank situation.

The A matrix must be full rank to satisfy a unique solution of the equation, so cases (1)–(5) are not included here. In consideration of the ground projection path of the aircraft moving along its trajectory, each set of three calibration point sources should not fall on the same line.

Each calibration point source can obtain two sets of observation data (forward and backward), so a three-calibration-source scheme is required to observe two calibration point sources. It is also necessary to ensure that the two sources are not located on the same parallel line parallel to the aircraft's trajectory. Normally, the aircraft runs along the track at a speed of 6.8 km/s, an orbital height about 800 km, FOV of 65°, and sampling frequency of 1 s. Therefore, the FOV is a circle with a diameter of 800 km $\times$ tan32.5° $\times$ 2 = 1019.31 km. The projection center of the adjacent frame is at a distance of 6.8 km/s $\times$ 1 s = 6.8 km, so the images overlap across a relatively large area.

According to the characteristics of the antenna, we initially assumed that the same θ angle of each antenna pattern had the same error value, then solved the pattern error of θ between 0° and 33°. As the aircraft flies near and far away from the target area, the observed θ angle of each antenna pattern gets smaller and then larger to traverse these values. As shown in Table III, when $\theta_1 = \theta_2 = \theta_3$, only $\varphi_1 \neq \varphi_2 \neq \varphi_3$ reveals the unique error solution. Thus, each θ angle to be solved requires three calibration point sources in different φ values. A schematic diagram of the positioning of calibration sources is given below.

As shown in Fig. 17, the ground calibration point sources were placed in the j column and k column, respectively. The j column in this case is located on the projection of the aircraft trajectory on the ground while the k column is parallel to the projected trajectory. The two columns of calibration sources are arranged cross-wise. The distance between two adjacent calibration point sources should be greater than 50 km to ensure that they are not in the same pixel unit.

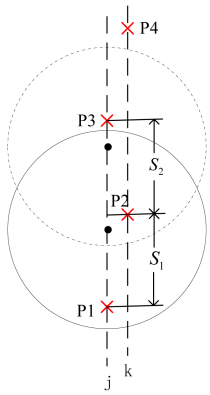

Fig. 17. 2D schematic diagram of calibration point source distribution.

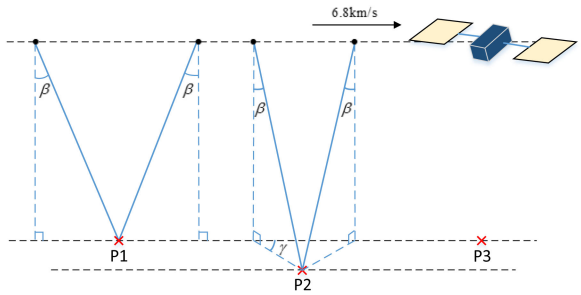

Fig. 18. 3D schematic diagram of project (Case 1).

For the purposes of practical application, the appropriate distance between calibration point sources should be selected according to terrain, ground conditions, and other relevant factors. The minimum observed elevation angle at which P2 can be obtained when the aircraft flies overhead is defined here as α. We analyzed three cases to solve the antenna pattern error and antenna position error at the elevation angle $\theta = \beta$.

1) $\alpha < \beta$. As shown in Fig. 18, before and after passing P1, the aircraft can obtain two sets of observed values ($\theta = \beta, \varphi = 0°$ and $\theta = \beta, \varphi = 180°$). Before and after passing P2, the aircraft can obtain another two sets of observed values ($\theta = \beta, \varphi = \gamma°$ and $\theta = \beta, \varphi = 180°$-$\gamma°$) for a total of four sets of observed values. The antenna pattern and position error can be calculated using any three of these four sets.
2) $\alpha = \beta$. As shown in Fig. 19, before and after passing P1, the aircraft can obtain two sets of observed values ($\theta = \beta, \varphi = 0°$ and $\theta = \beta, \varphi = 180°$). When passing P2, the aircraft can obtain only one more set ($\theta = \beta, \varphi = 90°$) for a total of three sets of observed values. The pattern error and position error of angle β can be calculated directly.
3) $\alpha > \beta$. In this case, the β angle of the point P2 is not observable, so the error cannot be solved.

It is worth noting that the proposed method can only be used to obtain the antenna pattern and the position error above the maximum value of the minimum θ angle among each calibration point source. It is best to set the calibration point sources as

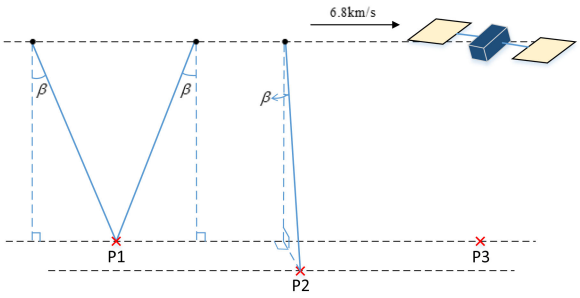

Fig. 19. 3D schematic diagram of project (Case 2).

close as possible to the projected trajectory of the aircraft on the ground to maximize the solution range.

VI. Conclusion

An in-orbit external antenna pattern and position error calibration method for synthetic aperture radiometers was developed in this study. The feasibility and accuracy of the proposed method were validated by simulation-based and experimental analyses. The layout of on-ground calibration point sources was explored and a feasible implementation scheme was established. Our results indicate that it is sufficient to adjust the power of the calibration point sources when SNR is 30 dB, and that the calibration requirements can initially be met with three calibration point sources. If better calibration effect is required, eight calibration point sources are sufficient. Nonrepeated and uniformed azimuth angles appear to be the optimal layout for operating the proposed method, however, adjustments can be made to suit the situation at hand.

The proposed method retains the advantages of external calibration while managing the in-orbit antenna error calibration that traditional internal calibration cannot resolve. The proposed method also does not require that the instrument be flipped. The proposed method has certain reference value for improving imaging quality and for application in practical engineering scenarios.

References

[1] D. M. Levine and J. C. Good, "Aperture synthesis for microwave radiometers in space," NASA, Washington, DC, USA, TM-85033, 1983.
[2] C. S. Ruf, C. T. Swift, A. B. Tanner, and D. M. Le Vine, "Interferometric synthetic aperture microwave radiometry for the remote sensing of the earth," *IEEE Trans. Geosci. Remote Sens.*, vol. 26, no. 5, pp. 597–611, Sep. 1988.
[3] J. L. Pawsey and R. N. Bracewell, *Radio Astronomy*. London, U.K.: Oxford Univ., 1955.
[4] P. J. Napier, A. R. Thompson, and R. D. Ekers, "The very large array: Design and performance of a modern synthesis radio telescope," *Proc. IEEE*, vol. 71, no. 11, pp. 1295–1320, Nov. 1983.
[5] M. Martàn-Neira *et al.*, "Microwave interferometric radiometry in remote sensing: An invited historical review," *Radio Sci.*, vol. 49, no. 6, pp. 415–449, 2014.
[6] B. Lambrigtsen, W. Wilson, A. Tanner, T. Gaier, C. Ruf, and J. Piepmeier, "Geostar—A microwave sounder for geostationary satellites," in *Proc. IEEE Int. Geosci. Remote Sens. Symp.*, vol. 2, 2004, pp. 777–780.
[7] A. B. Tanner *et al.*, "Initial results of the geostationary synthetic thinned array radiometer (GeoSTAR) demonstrator instrument," *IEEE Trans. Geosci. Remote Sens.,* vol. 45, no. 7, pp. 1947–1957, Jul. 2007.
[8] H. M. Barré, B. Duesmann, and Y. H. Kerr, "SMOS: The mission and the system," *IEEE Trans. Geosci. Remote Sens.*, vol. 46, no. 3, pp. 587–593, Mar. 2008.
[9] J. Font *et al.*, "SMOS: The challenging sea surface salinity measurement from space," *Proc. IEEE*, vol. 98, no. 5, pp. 649–665, May 2009.
[10] Y. H. Kerr *et al.*, "The SMOS mission: New tool for monitoring key elements of the global water cycle," *Proc. IEEE*, vol. 98, no. 5, pp. 666–687, May 2010.
[11] M. Martín-Neira and J. M. Goutoule, "MIRAS—A two-dimensional aperture-synthesis radiometer for soil-moisture and ocean-salinity observations," *ESA Bull.*, no. 92, pp. 95–104, 1997.
[12] K. D. McMullan *et al.*, "SMOS: The payload," *IEEE Trans. Geosci. Remote Sens.*, vol. 46, no. 3, pp. 594–605, Mar. 2008.
[13] I. Corbella, A. J. Gasiewski, M. Klein, V. Leuski, A. J. Francavilla, and J. R. Piepmeier, "On-board accurate calibration of dual-channel radiometers using internal and external references," *IEEE Trans. Microw. Theory Techn.*, vol. 50, no. 7, pp. 1816–1820, Jul. 2002.
[14] A. B. Tanner and C. T. Swift, "Calibration of a synthetic aperture radiometer," *IEEE Trans. Geosci. Remote Sens.*, vol. 31, no. 1, pp. 257–267, Jan. 1993.
[15] M. Martín-Neira, M. Suess, J. Kainulainen, and F. Martin-Porqueras, "The flat target transformation," *IEEE Trans. Geosci. Remote Sens.*, vol. 46, no. 3, pp. 613–620, Mar. 2008.
[16] I. Corbella, F. Torres, A. Camps, N. Duffo, and M. Vall-Llossera, "Brightness-temperature retrieval methods in synthetic aperture radiometers," *IEEE Trans. Geosci. Remote Sens.*, vol. 47, no. 1, pp. 285–294, Jan. 2009.
[17] W. Wei, "Modeling and calibration of the antenna position errors on synthetic aperture radiometer," M.S. thesis, Dept. Elect. & Inform. Eng., Huazhong Univ. Sci. Tech., Wuhan, China, 2013.
[18] I. Corbella, N. Duffo, M. Vall-Llossera, A. Camps, and F. Torres, "The visibility function in interferometric aperture synthesis radiometry," *IEEE Trans. Geosci. Remote Sens.*, vol. 42, no. 8, pp. 1677–1682, Aug. 2004.
[19] A. Colliander *et al.*, "Development and calibration of SMOS reference radiometer," *IEEE Trans. Geosci. Remote Sens.*, vol. 45, no. 7, pp. 1967–1977, Jul. 2007.
[20] J. Kainulainen and A. Colliander, "In-orbit performance of the SMOS reference radiometers-results from the early commissioning phase," in *Proc. 11th Specialist Meeting Microw. Radiometry Remote Sens. Environ.*, 2010, pp. 5–10.
[21] F. Torres *et al.*, "Denormalization of visibilities for in-orbit calibration of interferometric radiometers," *IEEE Trans. Geosci. Remote Sens.,* vol. 44, no. 10, pp. 2679–2686, Oct. 2006.
[22] Y. Li *et al.*, "FPASMR: A new instrument for future sea surface salinity measurement," in *Proc. IEEE Int. Geosci. Remote Sens. Symp.*, 2017, pp. 3560–3563.
[23] I. Corbella *et al.*, "Inter-element phase calibration in interferometric radiometers," in *Proc. IEEE Int. Symp. Geosci. Remote Sens.*, 2006, pp. 3976–3979.

Jiakun Wang was born in China, in 1992. She received the B.S. degree from the School of Remote Sensing Information Engineering, Wuhan University, Wuhan, China, in 2014, and the M.S. degree in information and communication engineering from the China Academy of Space Technology, Xi'an, China, in 2017.

Since 2017, she has been working as an Engineer with the Radar Detection Technology Research group, China Academy of Space Technology. Her research interests include synthetic aperture radiometer system, especially the calibration of the system.

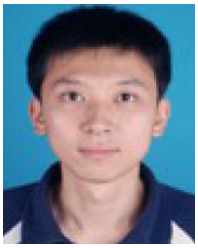

Yinan Li received the B.S and M.S degrees in electrical engineering from Xi'dian University, Xi'an, China, in 2007 and 2010, respectively.

He is currently a Senior Engineer with the China Academy of Space Technology, Xi'an, China. His research interests include the passive microwave remote sensing and the microwave radiometer design.

Wenxin Chen received the M.S degrees in system engineering from Xi'an Jiaotong University, Xi'an, China, in 1994.

He is currently a Chief Engineer with China Academy of Space Technology, Xi'an, China. His main research interests are the passive microwave remote sensing and the microwave radiometer design.

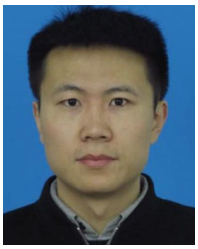

Pengju Jin received the B.S. degree in electronic information engineering from Northwestern Polytechnical University, Xi'an, China, in 2014, and the M.S. degree in electromagnetic field and microwave technology from China Academy of Space Technology, Xi'an, China, where he is currently working toward the Ph.D. degree in spacecraft communication technology.

His research interests include spacecraft communications, information theory, and sparse antenna array.

Hailiang Lu received the Ph.D. degree in the electromagnetic field and microwave technology from Huazhong University of Science and Technology, Wuhan, China, in 2016.

He is currently a Senior Engineer with the China Academy of Space Technology, Xi'an, China. His research interests include the passive microwave remote sensing, the passive microwave detection, and the radio frequency interference detection.

Xiaojiao Yang was born in Chongqing, China, in 1988. She received the M.S. degree in information and communication engineering from China Academy of Space Technology, Xi'an, China, in 2014.

In 2011, she joined the passive remote sensing group of China Academy of Space Technology. Since 2011, she has been supporting the instrument testing, mission operation, and calibration algorithm of 1D and 2D aperture synthesis radiometers. Her current research interests include data processing and research of calibration methods, devoted to the high-quality data products.

Guangnan Song received the B.S. and M.S. degrees in electrical engineering from Nanjing University of Science and Technology, Nanjing, China, in 2010 and 2013, respectively.

He is currently a Senior Engineer with the China Academy of Space Technology, Xi'an, China. His research interests include the passive microwave remote sensing and the microwave radiometer design.

Pengfei Li received the B.S. degree in electrical engineering from the Harbin Institute of Technology, Weihai, China, in 2012, and M.S. degree in electrical engineering from the China Academy of Space Technology, Xi'an, China, in 2015.

He is currently an Engineer with the China Academy of Space Technology. His research interests include microwave remote sensing, radiometer system design, and system calibration.

Hao Li received the B.S. degree in electrical engineering from Xi'dian University, Xi'an, China, in 2002, and the M.S. degree in information and communication engineering from the China Academy of Space Technology, Xi'an, China, in 2005.

He is currently a Professor with the China Academy of Space Technology. His research interests include the passive microwave remote sensing and the microwave radiometer design.

Rongchuan Lv received the B.S. and M.S. degrees in electrical engineering from Xi'dian University, Xi'an, China, in 2004 and 2007, respectively.

She is currently a Professor with the China Academy of Space Technology, Xi'an, China. Her research interests include the passive microwave remote sensing and the microwave radiometer design.